Enhanced Piezocatalytic Performance of BaTiO$_3$ Nanosheets with Highly Exposed {001} Facets

Journal Article

Author(s):
Tang, Qiao; Wu, Jiang; Kim, Donghoon; Franco, Carlos; Terzopoulou, Anastasia; Veciana, Andrea; Puigmarti-Luis, Josep; Chen, Xiang-Zhong; Nelson, Bradley J.; Pané, Salvador

Publication date:
2022-08-25

Permanent link:
https://doi.org/10.3929/ethz-b-000555906

Originally published in:
Advanced Functional Materials 32(35), https://doi.org/10.1002/adfm.202202180

Funding acknowledgement:
771565C - Highly Integrated Nanoscale Robots for Targeted Delivery to the Central Nervous System (EC)
192012 - Mechano-chromic, Voltage-sensitive Electrostimulators: Innovative Piezoelectric Biomaterials for Electro-stimulated Cellular growth (SNF)

ADVANCED FUNCTIONAL MATERIALS
www.afm-journal.de

Enhanced Piezocatalytic Performance of $BaTiO_3$ Nanosheets with Highly Exposed {001} Facets

Qiao Tang, Jiang Wu, Donghoon Kim, Carlos Franco, Anastasia Terzopoulou, Andrea Veciana, Josep Puigmartí-Luis, Xiang-Zhong Chen, Bradley J. Nelson, and Salvador Pané**

Piezocatalysis has gradually come into the limelight due to its great potential for solving energy shortages and environmental pollution problems. However, limited piezocatalytic efficiency is a severe bottleneck for its practical applications. Here, well-defined $BaTiO_3$ nanosheets with highly exposed {001} polar facets are successfully synthesized to enhance the piezocatalytic activity. The [001] piezoelectric polarization can drive the carriers to migrate to the surface along the out-of-plane direction. The polar surface provides abundant active sites for the piezocatalytic reaction. As a result, a superior piezocatalytic degradation ratio of organic pollutants is obtained with a high first-order rate constant *k* of 0.0835 min^{-1}, which is 2.7 times higher than the $BaTiO_3$ nanoparticles. Furthermore, $BaTiO_3$ nanosheets display an outstanding H_2 production capability, with the rate of 305 µmol g^{-1} h^{-1}, which is almost two times higher than that of $BaTiO_3$ nanoparticles. This work thus provides a novel and comprehensive strategy for designing high-performance piezocatalysts with an out-of-plane polarization, and also provides novel insights for the optimization of the piezocatalytic activity by regulating the polar facet of piezocatalysts.

1. Introduction

Piezocatalysis is a recently developed technology that exploits mechanical energy to trigger chemical reactions.[1] In a typical piezocatalytic process, an external mechanical stimulus (e.g., ultrasonic vibration, ball milling) applied to the catalyst forces its centroids of positive and negative charges to separate, generating an internal electric field that drives charge transfer from the catalysts to the surrounding medium to initialize chemical reactions.[2] Piezocatalysis has been explored for sterilization,[3] tumor treatment,[4] neurodegenerative therapy,[5] H_2 production,[6] pollutant degradation,[7] N_2 fixation,[8] and organic synthesis.[9] Among these applications, pollutant degradation, and H_2 production have gained increasing attention due to their prospects of solving increasingly severe energy and environmental problems through sustainable mechanical energy. Increased catalytic performance is key to translating piezocatalysts into practical applications, and one indispensable way to achieve this is to design and fabricate piezocatalysts with optimal catalytic activity.

An excellent piezocatalyst should display a high piezoelectric coefficient, superior deformability, a large surface area for exposure to mechanical impact, and abundant catalytic active sites.[10] These requirements impose significant challenges to the piezocatalysts currently used, such as nanoparticles and nanowires. For instance, nanoparticles usually suffer from a low deformation, which is crucial for the generation of a large piezoelectric potential. In contrast, nanowires can be highly deformable and usually shows the highest piezoelectric potential due to preferred crystalline (and thus polarization) orientation. However, nanowires can only provide limited active sites for the catalytic reactions. In view of the shortcomings of both nanowires and nanoparticles, efforts have been recently dedicated to exploring 2D piezoelectric materials, which are considered to exhibit high deformability and large surface area. For example, Zhang et al. reported that ZnS nanosheets[10] exhibited superior piezocatalytic performance due to their excellent flexibility and large surface area for receiving mechanical impact. Subsequently, other 2D piezoelectric materials, such as BiOCl,[11] $g\text{-}C_3N_4$,[12]

Q. Tang, J. Wu, D. Kim, C. Franco, A. Terzopoulou, A. Veciana, X.-Z. Chen, B. J. Nelson, S. Pané
Institute of Robotics and Intelligent Systems
ETH Zurich
Tannenstrasse 3, 8092 Zurich, Switzerland
E-mail: jianwu@ethz.ch; vidalp@ethz.ch

J. Puigmartí-Luis
Department of Physical Chemistry
University of Barcelona
Martí i Franquès, 1, 08028 Barcelona, Spain

J. Puigmartí-Luis
ICREA
Institució Catalana de Reserca i Estudis Avançats
Pg. Lluís Companys 23, 08010 Barcelona, Spain

The ORCID identification number(s) for the author(s) of this article can be found under https://doi.org/10.1002/adfm.202202180.

DOI: 10.1002/adfm.202202180

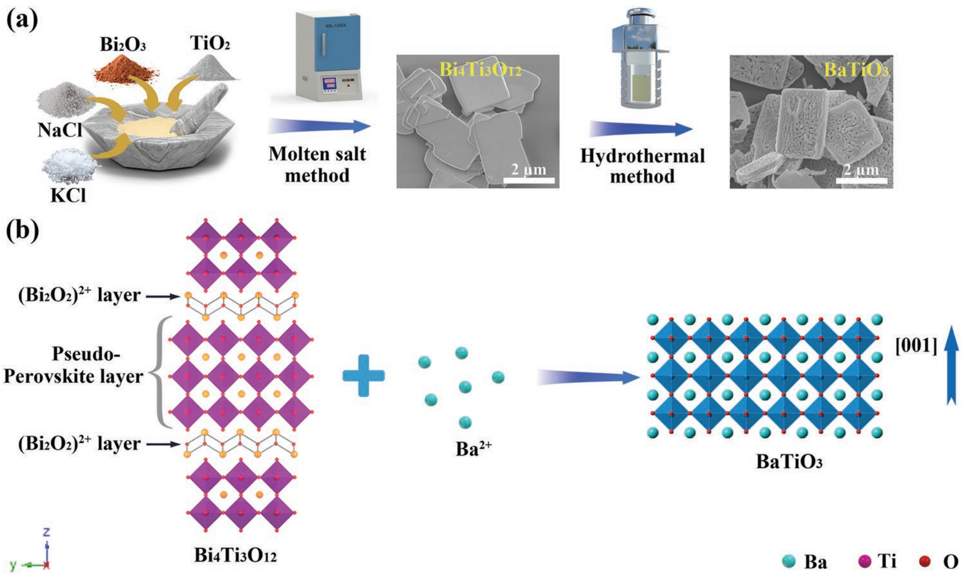

Figure 1. Preparation of BTO NSs: a) Schematic illustration of the synthetic route. b) Diagram of the $Bi_4Ti_3O_{12}$-to-$BaTiO_3$ transformation.

and $Bi_4Ti_3O_{12}$[13] have also been reported. These 2D piezocatalysts possess in-plane polarization, along whose direction the strongest electric fields are assumed to be generated under mechanical vibration. Driven by the in-plane piezoelectric fields, the charge carriers travel a long way toward the lateral sides to participate in catalytic reactions. Note that a long traveling distance will lower the catalytic performance due to an increased probability of recombination of charge carriers. Besides, only a small surface of active sites is available on the lateral sides. To overcome these limitations, piezocatalysts with increased active sites and reduced carriers migration distance would significantly promote the piezocatalytic reaction performance. A way to address these features is the realization of 2D piezoelectric catalysts with out-of-plane polarization through crystallographic engineering. Presumably, the migration distance along the thickness direction is much shorter than the in-plane direction. A shorter migration length will increase catalytic performance, as indicated by previous studies.[14] Besides, there will be plenty of active sites on the flat surface of the 2D materials.

Here, we report for the first time the synthesis of uniform $BaTiO_3$ nanosheets with out-of-plane polarization. The crystal structure investigation demonstrates that the as-prepared $BaTiO_3$ are single-crystalline nanosheets with highly exposed {001} facets, implying a superior polarization along the out-of-plane direction. Owing to this unique property, $BaTiO_3$ nanosheets exhibit a superior piezocatalytic activity for organic pollutant degradation and H_2 production, surpassing the catalytic action of the previously reported piezoelectric nanoparticles.

2. Results and Discussion

2.1. Fabrication and Structure Characterization

As a layer-structured perovskite, $Bi_4Ti_3O_{12}$ can be easily fabricated into nanosheets. Therefore, we employed $Bi_4Ti_3O_{12}$ nanosheets as templates, and Ti sources for the growth of $BaTiO_3$. As illustrated in **Figure 1**a, $Bi_4Ti_3O_{12}$ nanosheets were synthesized by a molten salt method.[15] After 2 h of annealing, rectangular $Bi_4Ti_3O_{12}$ nanosheets with smooth surfaces were obtained (Figure S1a, Supporting Information). XRD patterns (Figure S1b, Supporting Information) confirmed that the main exposed facet is {001}. Rectangular $BaTiO_3$ nanosheets (denoted as BTO NSs) were obtained by reacting the $Bi_4Ti_3O_{12}$ nanosheets with $BaCl_2$ under hydrothermal conditions, as illustrated in Figure 1b. During the in situ hydrothermal reaction, abundant $Ti(OH)_6{}^{2-}$ fragments can be formed by the dissolution of $Bi_4Ti_3O_{12}$.[16] Then, Ba^{2+} ions gradually react with $Ti(OH)_6{}^{2-}$ fragments and crystallize into $BaTiO_3$ by the following process:

$$Ti(OH)_6^{2-} + Ba^{2+} \rightarrow BaTiO_3 + 3H_2O \quad (1)$$

EDX maps show that Ba, Ti, and O are uniformly distributed in BTO NS (**Figure 2**a). Further information on the purity of BTO NSs was evaluated by XPS. As depicted in Figure S2a (Supporting Information), no elements other than *C* (background), Ba, Ti, and O were observed in the full XPS spectrum. The high-resolution spectrum of Ba 3d displays two split peaks, Ba $3d_{5/2}$ at 778.5 eV and Ba $3d_{3/2}$ at 793.8 eV, which are referred to as Ba^{2+} (Figure S2b, Supporting Information).[17] The Ti 2p peaks can be resolved into two peaks at 457.7 and 463.5 eV, which correspond to the Ti $2p_{3/2}$ and Ti $2p_{1/2}$ of Ti^{4+} (Figure S2c, Supporting Information).[17,18] The broad peak of O 1 s spectrum (Figure S2d, Supporting Information) can be resolved into two separated peaks of 529.1 and 530.9 eV, which are ascribed to lattice oxygen and surface absorbed oxygen, respectively.[17b] The detection of Ba and Ti, as well as the absence of Bi, indicates the complete transformation of $Bi_4Ti_3O_{12}$ to $BaTiO_3$.

XRD was carried out to provide fingerprint evidence that BTO NSs are in the correct crystalline phase. As shown in Figure 2b, all the diffraction peak positions correspond well with pure $BaTiO_3$ (JCPDS data No. 05–0626). A distinctly asymmetric peak was observed at $\approx 2\theta = 45°$, indicating the existence

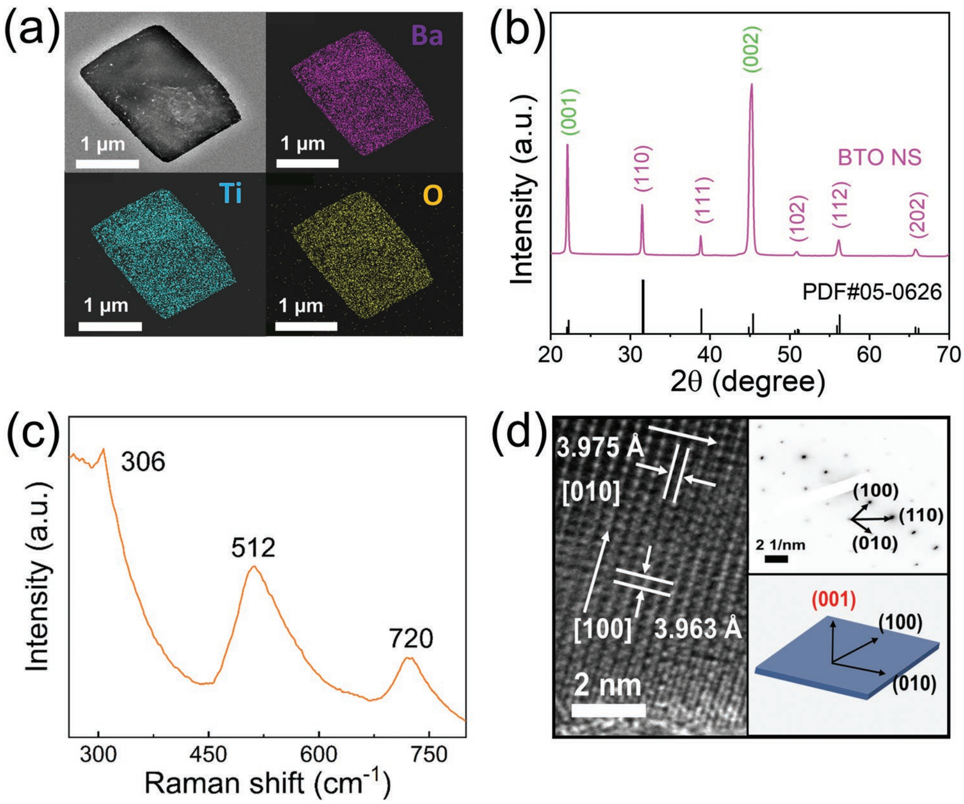

Figure 2. Characterization of BTO NSs: a) TEM with corresponding EDX mapping images, b) XRD pattern, c) Raman spectra, and d) HRTEM image and SAED pattern.

of a tetragonal phase in BTO NSs (Figure S3, Supporting Information). Notably, the relative intensity ratio of the (001) peak to that of the (110) peak is 1.46, a value much higher than the standard ratio 0.25. This result suggests that the as prepared BTO samples grow with a preferred <001> orientation, resulting in highly exposed {001} facets. Raman spectroscopy (Figure 2c) reveals the tetragonal symmetry of $BaTiO_3$, as evidenced by the weak peak at 306 cm^{-1} representing the scattering mode E(3TO) + E(2LO) + B_1, confirming the piezoelectric nature of the as-prepared BTO samples.[19] The high-resolution transmission electron microscope (HRTEM) image (Figure 2d) viewed from the *c*-axis (out-of-plane) direction displays two sets of fringes with an interplanar distance of 3.963 ± 0.009 and 3.957 ± 0.015 Å, corresponding to the spacing of (100)/(010) crystal planes of tetragonal $BaTiO_3$. The corresponding selected area electron diffraction (SAED) displays a set of ordered diffraction spots, suggesting the single-crystalline characteristic of BTO NSs. The diffraction spots could be well indexed to (100), (010), and (110) facets. The evidence clearly proves that we have synthesized tetragonal-BTO NSs with highly exposed {001} facets.

2.2. Piezoelectric Property

The piezoelectric response of the BTO NSs was investigated along the out-of-plane and in-plane directions using PFM, respectively. Along the out-of-plane direction (perpendicular to the NS), both PFM amplitude (**Figure 3**a) and phase images (Figure 3c) present a distinct contrast with the background, representing a strong piezoelectric response. However, only very weak contrast is observed along the in-plane direction (Figure 3b,d). The intensity distribution of the amplitude signal is displayed in Figure 3e. After subtracting the background signal (shaded area), the most probable distribution of piezoresponse amplitude for out-of-plane is ≈24.5 pA, which is much higher than that of the in-plane direction (≈0.5 pA). The local piezoelectric response and polarization switching behaviors in the out-of-plane mode were investigated by sweeping a DC voltage. As shown in Figure 3f, a typical hysteresis loop with 180° phase-reversal and a well-shaped amplitude butterfly loop were obtained. The PFM measurements confirm that the BTO NSs possess a strong piezoelectric polarization along the out-of-plane direction. This feature is consistent with the highly exposed {001} facet in the BTO NSs, as previously suggested by the XRD and HRTEM.

2.3. Piezocatalytic Activity

Given the highly exposed {001} polar facet and superior out-of-plane piezoelectric property, promising piezocatalytic activity of these BTO NSs is expected. To fully investigate the piezocatalytic activity, degradation of organic pollutants and decomposition of water under ultrasonic vibration was performed. As shown in Figure S4 (Supporting Information), the peak intensities of the model pollutants in the UV–vis absorption spectra decrease significantly with reaction time. It is reported that

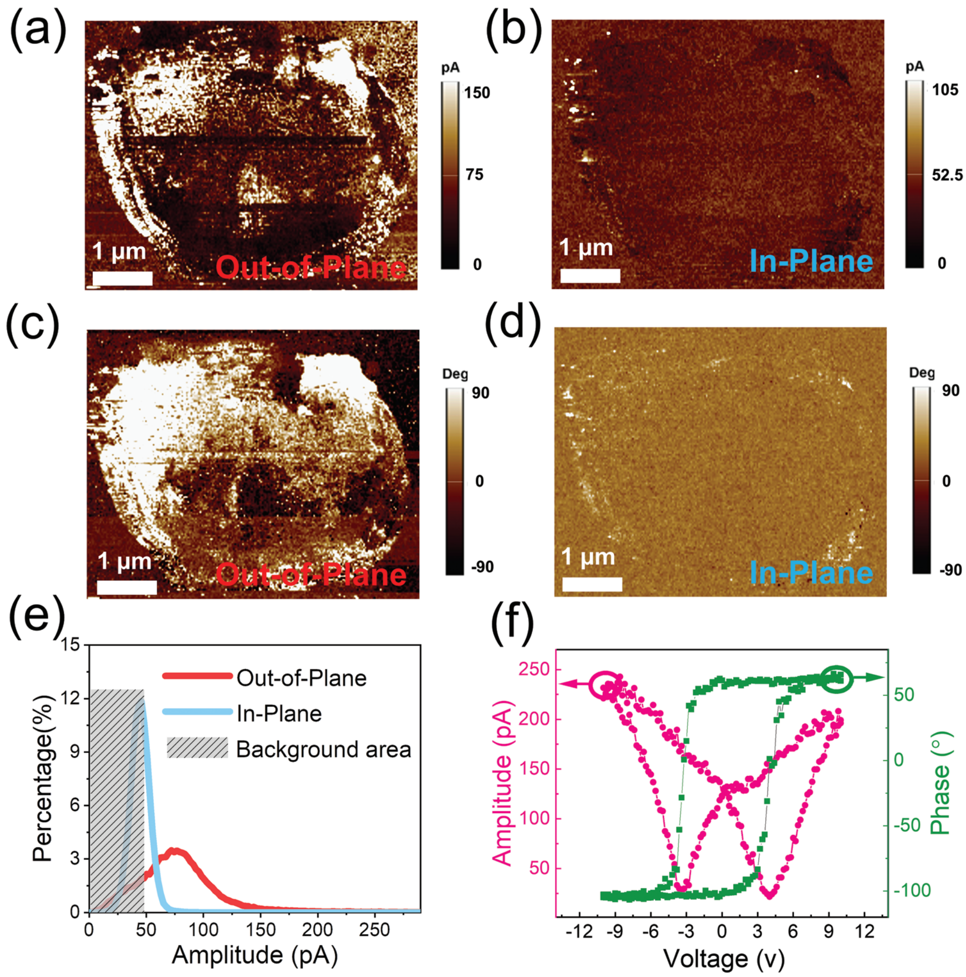

Figure 3. Piezoelectric properties of BTO NSs: a) Out-of-plane, and b) in-plane PFM amplitude images. c) Out-of-plane, and d) in-plane PFM phase images. e) Distribution of the amplitude signal. Statistics were made with at least 60 000 data points for each part. f) Out-of-plane amplitude butterfly loop and phase hysteresis loop.

most organic pollutants can be degraded to smaller, harmless products.[20] In contrast, negligible degradation of the pollutants was observed under ultrasonic stimulation when no BTO NSs were added (Figure S5, Supporting Information), ruling out the possibility that ultrasonic cavitation induced dye degradation. The relative concentration change (C/C_0) over time and the pseudo-first-order rate constant k extracted from these experiments are presented in **Figure 4**a,b. Specifically, the degradation efficiency of MO, MB, phenol, BPA, TH, and RhB reach 97.1%, 91.3%, 63.1%, 61.3%, 54.9%, and 47.2%, with a rate of 0.0835, 0.0638, 0.0265, 0.026, 0.0224, and 0.0156 min^{-1}, respectively. For comparison, the degradation experiments with BTO nanoparticles (denoted as BTO NPs, also in tetragonal phase, as evidenced in Figure S6, Supporting Information) were carried out. The piezocatalytic degradation experiments of MO over BTO NPs and NSs are shown in Figure 4c. While it takes only 40 min for the BTO NSs to degrade >97% of the dye, the BTO NPs need more than 120 min to achieve this. To clarify the effect of specific surface area on piezocatalytic activity, the nitrogen (N_2) adsorption/desorption isotherms were measured. As shown in Figure S7 (Supporting Information), the isotherms show a single and narrow hysteresis loop. The specific surface areas of BTO NSs and NPs were calculated to be 11.9 and 10.3 m^{-2} g^{-1}, respectively. The small difference in BET surface suggests that the enhanced piezocatalytic activity of BTO NSs is not caused by the larger specific surface area in NSs. With the same weight concentration of catalysts, the k value for the BTO NSs (0.0835 min^{-1}) is 2.7 times higher than that for BTO NPs (0.0307 min^{-1}). To evaluate the reusability of BTO NSs, the MO degradation experiment was repeated with recycled samples (Figure S8, Supporting Information). Similar piezocatalytic activities were observed in three consecutive cycles, demonstrating the stability of the BTO NSs catalyst.

The piezocatalytic H_2 production experiment with BTO NSs and BTO NPs was also performed. As shown in Figure 4d, the H_2 production rate of the BTO NSs is 305 µmol g^{-1} h^{-1}, which is twice that of the BTO NPs (157 µmol g^{-1} h^{-1}). We repeated the H_2 production experiments three times (Figure S9, Supporting Information), and observed a stable H_2 production activity, indicating the good recyclability of BTO NSs. Methanol is usually added to the catalytic reaction system as a hole scavenger to accelerate the reaction.[21] The BTO NSs displayed

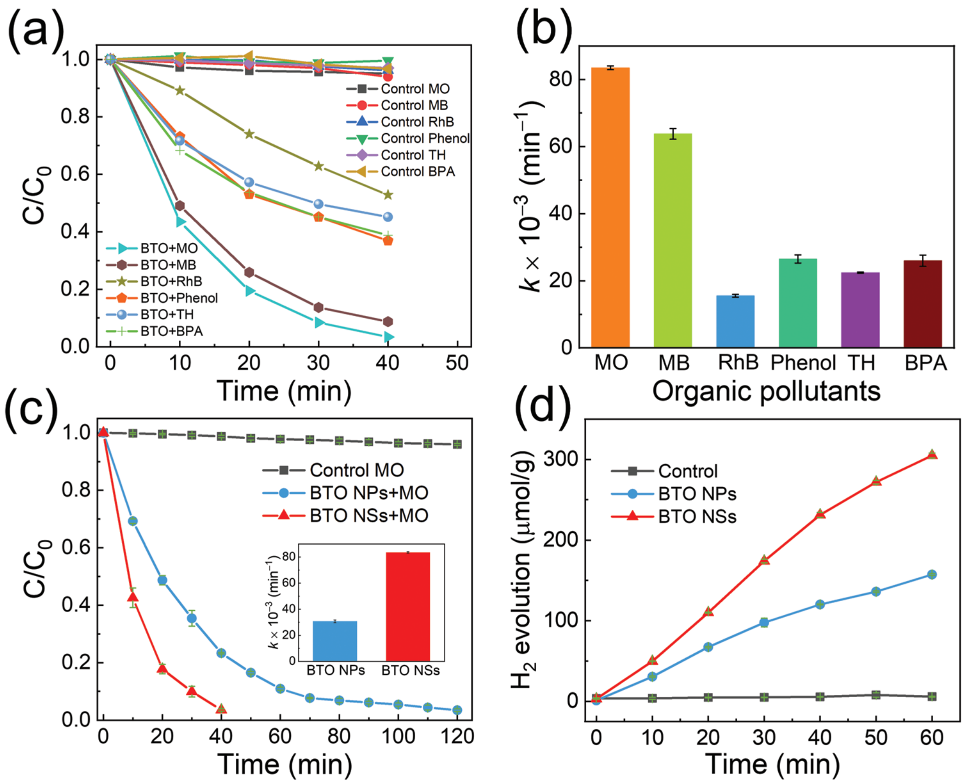

Figure 4. The piezocatalytic pollutant degradation and H_2 production activity: a) Degradation dynamic curves, and b) corresponding first-order rate constants of the degradation reaction when BTO NSs are used as piezocatalysts. Comparison of the performance of BTO NSs and BTO NPs in c) MO degradation efficiency, and d) H_2 evolution from pure water under ultrasonic vibration. Each data point was measured at least 3 times. The data are presented as mean value ± the SD.

a dramatically enhanced H_2 evolution activity with a rate of 1486 µmol g^{-1} h^{-1} (Figure S10, Supporting Information), which is approximately five times higher than that of pure water. To our knowledge, this value is also much higher than that of the most reported 2D piezocatalysts, such as CdS,[22] Bi_2WO_6,[23] $BiFeO_3$,[24] and MoS_2[25] (Table S1, Supporting Information). These results strongly suggest that the introduction of out-of-plane polarization is an effective approach to enhance the piezocatalytic activity.

2.4. Kinetics and Mechanism

To gain an insight into the piezocatalytic mechanism, we performed scavenger-quenching experiments on the main reactive species. As shown in **Figure 5**a,b, the degradation of MO is significantly inhibited upon the addition of tert-butyl alcohol (TBA) or benzoquinone (BQ), while moderate weakening is observed by adding disodium ethylenediaminetetraacetate (EDTA-2Na, trapping h^+). The above results suggest that $\bullet O_2^-$ and •OH radicals are the most probable reactive species responsible for the degradation of organic dye, which is in line with several recent reports.[26] However, it has been reported that under certain circumstances, BQ can also react with •OH in addition to $\bullet O_2^-$.[27] In order to further confirm the predominant radical produced during piezocatalysis, the concentration of $\bullet O_2^-$, •OH radicals, and H_2O_2 were investigated by the UV–vis absorption spectra or fluorescence spectra.[28] As shown in Figure S11a (Supporting Information), the absorption peak intensity of NBT solution at 259 nm decreases with the reaction time, indicating a constant generation of $\bullet O_2^-$.[28b] Based on the rule that 1 mol NBT can react with 4 mol $\bullet O_2^-$,[29] the concentration of $\bullet O_2^-$ radicals is quantified. As shown in Figure 5c, the average evolution rate of $\bullet O_2^-$ is 8.14 µmol g^{-1} h^{-1}. Furthermore, 2-hydroxyterephthalic acid was employed to detect the concentration of •OH radicals, as •OH can react with terephthalic acid and emit fluorescence at 425 nm.[28a] With the application of ultrasonic vibration, progressively enhanced fluorescence intensity was observed, suggesting the continuous production of •OH radicals (Figure S11b, Supporting Information). According to the linear relationship between •OH concentration and fluorescence intensity,[28a] the generation rate of •OH was determined to be 150.21 µmol g^{-1} h^{-1} (Figure 5c), which is much higher than that of the reported BTO nanocubes (≈40 µmol g^{-1} h^{-1}).[28b] The concentration of •OH is also much higher than that of $\bullet O_2^-$, indicating that the former plays a more important role in our piezocatalytic process. Similarly, the concentration of H_2O_2 was examined by iodide method (Figure S11c, Supporting Information).[28c] The average H_2O_2 production rate was calculated to be 125.59 µmol g^{-1} h^{-1} based on the standard curve (Figure S12, Supporting Information). In comparison, the evolution rates of $\bullet O_2^-$, •OH radicals, and H_2O_2 of BTO NPs are 6.55, 107.99, and 79.30 µmol g^{-1} h^{-1} (Figure S13, Supporting Information), which are all lower than those of BTO NSs.

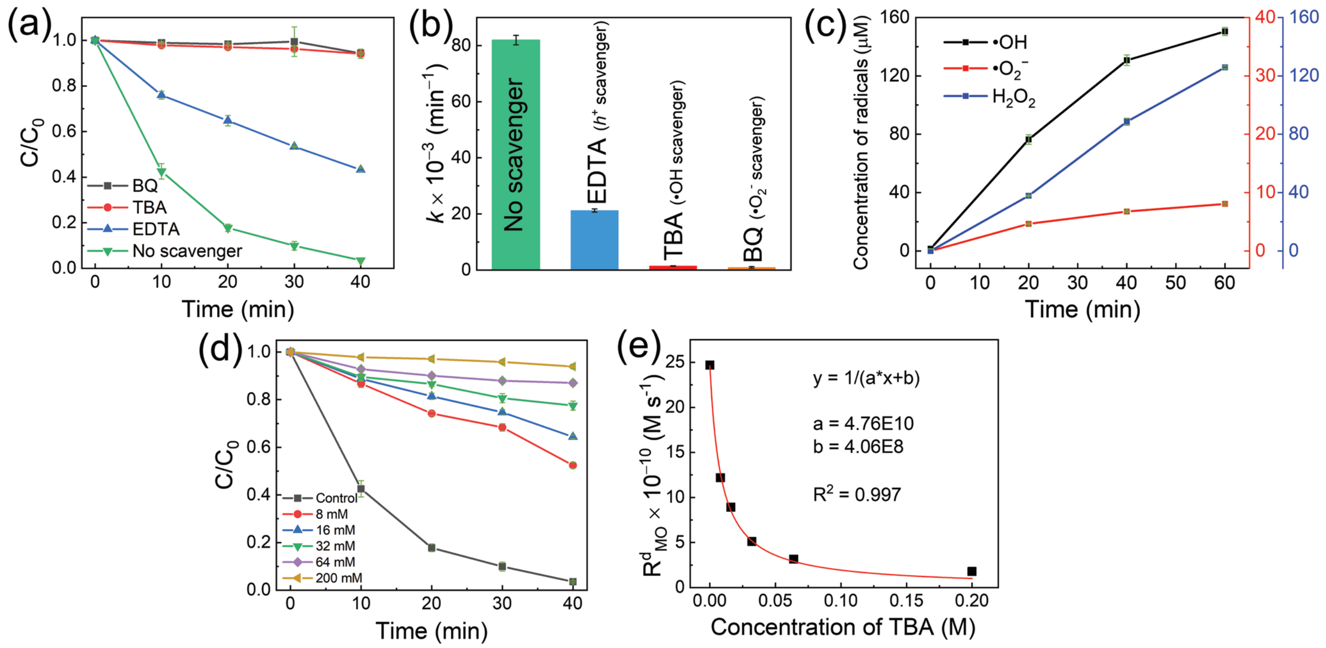

Figure 5. Piezocatalytic reactivity of BTO NSs for free radical generation: a) MO degradation efficiency with and without free radical scavengers, and b) corresponding first-order rate constants. c) Concentration dynamic curves of generated $\bullet O_2^-$, •OH, and H_2O_2. d) Effect of •OH scavenger dosage on MO degradation, and e) degradation rate of MO as a function of •OH scavenger dosages over BTO NSs. Each data point was measured at least three times. The data are presented as mean value ± the SD.

Considering that •OH made a major contribution to the piezocatalytic degradation of MO, we further evaluated its inhibitory performance by the steady-state approximation analysis method,[30] where various doses of •OH scavenger (TBA) were introduced into the degradation process (Figure 5d,e). According to the literature,[28b] the generation rate of •OH ($R^f_{\cdot OH}$) can be determined by Equation 2.

$$R^{\mathrm{f}}_{\cdot\mathrm{OH}} = \frac{k_{\mathrm{TBA},\cdot\mathrm{OH}}}{a k_{\mathrm{MO}} C_{\mathrm{MO}}} \quad (2)$$

Here, $k_{\mathrm{TBA},\cdot\mathrm{OH}}$ (6×10^8 M^{-1} s^{-1}), and k_{MO} (≈2×10^{10} M^{-1} s^{-1}) are second-order rate constants of •OH with TBA and MO, respectively.[28b,31] The value of "a" can be calculated by considering the relationship between the concentration of TBA (C_{TBA}) and degradation rate of MO (R^d_{MO}) with the following equation: $R^d_{MO} = \frac{1}{aC_{TBA}+b}$. As shown in Figure 5e, the value of "a" is determined to be 4.76×10^{10} M^{-2} s. Hence, the generation rate of •OH ($R^f_{\cdot OH}$) is calculated to be 3.44×10^{-6} M s^{-1}, which is much higher than that of the reported BTO nanocubes (2.3×10^{-8} M s^{-1}).[28b] These results show that BTO NSs with highly exposed {001} facets can efficiently activate the generation of •OH and H_2O_2.

Based on the above results, a mechanism to explain the enhanced piezocatalytic activity of BTO NSs is proposed in **Figure 6**. The finite element simulation demonstrated that BTO

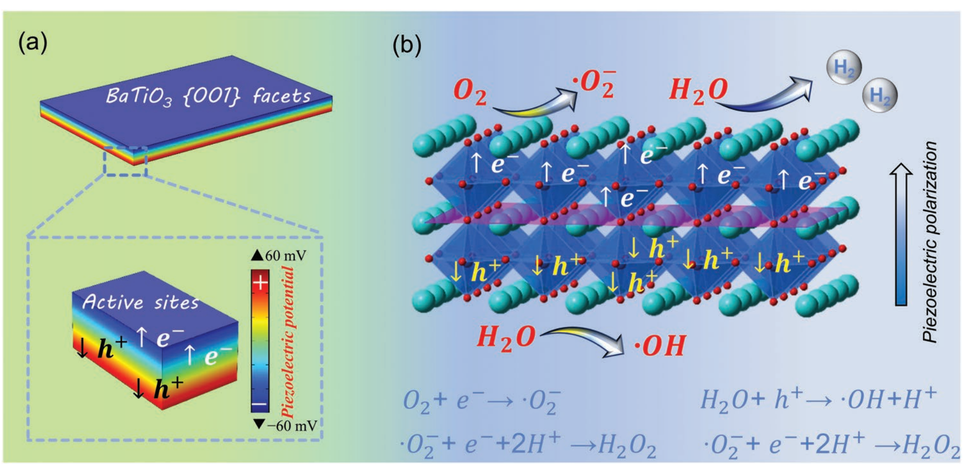

Figure 6. Piezocatalytic mechanism diagram of BTO NSs: a) Illustration of out-of-plane polarization process and highly exposed {001} facets. b) Mechanism diagram of charge transfer and subsequent dye degradation and H_2 production.

NSs exhibit a noticeable out-of-plane piezoelectric response, which can drive electrons and holes to separate quickly along the direction perpendicular to the nanosheets. The out-of-plane migration path greatly reduces the carrier migration distance. In addition, the highly exposed {001} facets function as catalytic reaction surfaces, providing abundant active sites. Hence, the enriched carriers and the shortened migration distances collectively lead to the boost in piezocatalytic activity of BTO NSs.

3. Conclusions

In summary, well-defined $BaTiO_3$ nanosheets with highly exposed {001} facets were first synthesized via a template-based hydrothermal method, and their piezocatalytic activity was fully investigated. Benefiting from the superior out-of-plane piezoelectric property and highly exposed {001} facets, the as-prepared $BaTiO_3$ nanosheets showed excellent piezocatalytic performance for pollutant degradation and H_2 production, which is much higher than that of the nanoparticle counterparts and most of the two-dimension piezocatalysts. This work provides a novel and efficient route to prepare high-performance piezocatalyst with out-of-plane polarization, and will open a new avenue for improving piezocatalytic activity.

4. Experimental Section

$BaTiO_3$ nanosheets were prepared using a template-based hydrothermal method in which $Bi_4Ti_3O_{12}$ nanosheets were used as the templates and Ti source. The specific process is described in the following sections.

Synthesis of $Bi_4Ti_3O_{12}$ Nanosheets as Templates: $Bi_4Ti_3O_{12}$ nanosheet templates were prepared using a one-step molten salt synthesis method.[15] First, 3.625 g of NaCl and 4.659 g of KCl were taken as cosolvents, and ground for 10 min in an agate mortar. Next, stoichiometric amounts of Bi_2O_3 and TiO_2 nanopowders were added as starting materials at a molar ratio of NaCl:KCl:Bi_2O_3:TiO_2 = 62.5:62.5:5:7.5. This mixture was ground thoroughly for 1.5 h and transferred to a corundum crucible. Subsequently, the synthesis was performed in a furnace at 700 °C for 2 h (heating rate: 10 °C min^{-1}). After naturally cooling to room temperature, the obtained precipitates were washed with deionized water and ethanol several times and dried at 70 °C overnight.

Synthesis of $BaTiO_3$ Nanosheets: The conversion reaction of $Bi_4Ti_3O_{12}$ to $BaTiO_3$ nanosheets was carried out through a hydrothermal method. Specifically, $Bi_4Ti_3O_{12}$ was used both as the template and Ti source, while $BaCl_2\cdot 2H_2O$ was employed as the Ba source. In addition, sodium oleate (NaOL) was added to regulate the morphology of the $BaTiO_3$ nanostructures. First, 0.12 g of NaOL was dissolved in 160 mL of 12 M NaOH aqueous solution and stirred for 30 min. Next, 2.198 g of $BaCl_2\cdot 2H_2O$ and 0.4 g of $Bi_4Ti_3O_{12}$ nanosheets were added and stirred for another 1.5 h. The final dispersion was poured into a 200 mL Teflon autoclave and heated at 240 °C for 20 h. Finally, the precipitate was washed with 2 M HNO_3 solution and ethanol several times and dried at 70 °C overnight to obtain $BaTiO_3$ nanosheets.

Material Characterization: The crystalline phase was confirmed by X-ray diffraction (XRD, Bruker AXS D8 Advance, Cu Ka). Scanning electron microscopic (SEM) images were obtained on a JSM-7100F electron microscope. Raman spectrum was obtained on a laser micro-Raman spectrometer (Renishaw inVia). Transmission electron microscopic (TEM) images and energy-dispersive X-ray (EDX) data were recorded using FEI Talos F200X (Chem S/TEM) operated at 150 kV. X-ray photoelectron spectroscopy (XPS) spectrum was conducted on a Phoibos 150 analyzer (SPECS EAS10P GmbH). The Brunauer–Emmett–Teller (BET) specific surface area (SBET) of the samples were determined by nitrogen adsorption on an ASAP 2020 nitrogen adsorption apparatus (Micromeritics Instruments). Piezoresponse force microscopic (PFM) measurements were characterized by a commercial atomic force microscope (NT-MDT Ntegra Prima).

Piezocatalytic Performance: The piezocatalytic activity was evaluated by the degradation of organic pollutants and decomposition of water. A cooled ultrasonic cleaner (Bandelin SC-255, 180 W, 35 kHz) was employed to provide mechanical vibration. To avoid interference from photocatalysis and pyrocatalysis, the catalytic experiments were performed in the dark at 25 °C.

For the degradation measurements, 50 mg of $BaTiO_3$ was dispersed in 50 mL of 2 mg L^{-1} organic pollutants aqueous solution (methylene orange (MO), methylene blue (MB), rhodamine B (RhB), bisphenol A (BPA), tetracycline hydrochloride (TH), and phenol). The suspension was continuously stirred in the dark for 30 min to reach the adsorption–desorption equilibrium. Subsequently, the dispersion was irradiated by ultrasonic vibration. At regular intervals, aliquots were taken from the reactor and the dye concentration was determined with a UV–vis spectrophotometer (Tecan Infinite 200 Pro).

For H_2 production, 50 mg of $BaTiO_3$ was added to 50 mL of deionized water or a mixture of methanol/deionized water (1:9). The suspension was continuously purged with Ar for 10 min to remove air. Mechanical vibration was then applied. The amount of evolved H_2 was evaluated by a gas chromatograph (Shimadzu GC 2014) with Ar as a carrier gas.

Detection of Free Radicals: To reveal the active species participating in the piezocatalytic process, *tert*-butyl alcohol was introduced (0.2 M, TBA), benzoquinone (0.15 M, BQ), and disodium ethylenediaminetetraacetate (0.2 M, EDTA-2Na) into the catalytic system as the scavengers of hydroxyl radicals (•OH), superoxide radicals ($\bullet O_2^-$), and holes (h^+), respectively. The amount of •OH, $\bullet O_2^-$, and H_2O_2 generated under mechanical vibration was determined by terephthalic acid photoluminescence (TA-PL),[28a,32] nitroblue tetrazolium (NBT) transmission,[28b] and iodide method,[28c] respectively.

COMSOL Simulation: The piezoelectric potential in BTO NSs was simulated by the finite element method with the aid of COMSOL Multiphysics software package. During the simulation, the pressure induced by ultrasonic cavitation was set as ≈10^8 Pa, the size was set the same as the prepared BTO samples (length = 2 µm, width = 1.5 µm, and thickness = 100 nm). The spontaneous polarization of BTO was oriented along the *z*-axis.

Statistical Analysis: Each data point in the dye degradation, H_2 production, and free radicals detection experiments was measured at least three times. The data were presented as mean ± standard deviation (SD).

Supporting Information

Supporting Information is available from the Wiley Online Library or from the author.

Acknowledgements

This work was financed by the ERC Consolidator Grant (No. 771565) and the Swiss National Science Foundation (Project No. 192012). The authors would like to thank Lydia Zehnder from the Institute for Geochemistry and Petrology at ETH for her support on XRD measurements, the Scientific Center for Optical and Electron Microscopy (ScopeM) and FIRST laboratory at ETH for its technical support, Dr. Ni Qin from Sun Yat-Sen University for her discussion in PFM, and Dr. Artur Braun from the Swiss Federal Laboratories for Materials Science and Technology (EMPA) for his support on gas chromatograph tests. The gas chromatograph test station used in this work was funded by the Swiss National Science Foundation program R'Equip project # 121306. Q.T. acknowledges financial support from the China Scholarship Council (No. 201806780021).

Open access funding provided by Eidgenossische Technische Hochschule Zurich.

Conflict of Interest

The authors declare no conflict of interest.

Data Availability Statement

The data that support the findings of this study are available from the corresponding author upon reasonable request.

Keywords

{001} facet, $BaTiO_3$ nanosheets, dye degradation, H_2 production, piezocatalyses

Received: February 23, 2022
Revised: May 18, 2022
Published online: June 23, 2022

[1] a) M. Wang, B. Wang, F. Huang, Z. Lin, *Angew. Chem., Int. Ed.* **2019**, *58*, 7526; b) S. Tu, Y. Guo, Y. Zhang, C. Hu, T. Zhang, T. Ma, H. Huang, *Adv. Funct. Mater.* **2020**, *30*, 2005158.
[2] a) X. Wang, *Nano Energy* **2012**, *1*, 13; b) R. Su, Z. Wang, L. Zhu, Y. Pan, D. Zhang, H. Wen, Z. D. Luo, L. Li, F. t. Li, M. Wu, *Angew. Chem.* **2021**, *133*, 16155.
[3] a) D. Xia, Z. Tang, Y. Wang, R. Yin, H. He, X. Xie, J. Sun, C. He, P. K. Wong, G. Zhang, *Chem. Eng. J.* **2020**, *400*, 125894; b) M. Wu, Z. Zhang, Z. Liu, J. Zhang, Y. Zhang, Y. Ding, T. Huang, D. Xiang, Z. Wang, Y. Dai, *Nano Today* **2021**, *37*, 101104.
[4] a) P. Wang, Q. Tang, L. Zhang, M. Xu, L. Sun, S. Sun, J. Zhang, S. Wang, X. Liang, *ACS Nano* **2021**, *15*, 11326; b) F. Mushtaq, H. Torlakcik, M. Hoop, B. Jang, F. Carlson, T. Grunow, N. Läubli, A. Ferreira, X. Z. Chen, B. J. Nelson, *Adv. Funct. Mater.* **2019**, *29*, 1808135.
[5] a) M. Hoop, X.-Z. Chen, A. Ferrari, F. Mushtaq, G. Ghazaryan, T. Tervoort, D. Poulikakos, B. Nelson, S. Pané, *Sci. Rep.* **2017**, *7*, 4028; b) X.-Z. Chen, J.-H. Liu, M. Dong, L. Müller, G. Chatzipirpiridis, C. Hu, A. Terzopoulou, H. Torlakcik, X. Wang, F. Mushtaq, *Mater. Horiz.* **2019**, *6*, 1512.
[6] a) G. Yang, Q. Chen, W. Wang, S. Wu, B. Gao, Y. Xu, Z. Chen, S. Zhong, J. Chen, S. Bai, *ACS Appl. Mater. Interf.* **2021**, *13*, 15305; b) Z. Zhao, L. Wei, S. Li, L. Zhu, Y. Su, Y. Liu, Y. Bu, Y. Lin, W. Liu, Z. Zhang, *J. Mater. Chem. A* **2020**, *8*, 16238.
[7] a) J. Wu, N. Qin, D. Bao, *Nano Energy* **2018**, *45*, 44; b) F. Mushtaq, X. Chen, M. Hoop, H. Torlakcik, E. Pellicer, J. Sort, C. Gattinoni, B. J. Nelson, S. Pané, *iScience* **2018**, *4*, 236.
[8] a) X. Dai, L. Chen, Z. Li, X. Li, J. Wang, X. Hu, L. Zhao, Y. Jia, S.-X. Sun, Y. Wu, *J. Colloid Interf. Sci.* **2021**, *603*, 220; b) M. Frank, Y. Bulut, L. Czympiel, R. Weißing, V. Nahrstedt, M. Wilhelm, M. Grosch, A. Raauf, A. Verma, T. Fischer, *Nanotechnology* **2021**, *32*, 465601.
[9] a) C. Schumacher, J. G. Hernández, C. Bolm, *Angew. Chem., Int. Ed.* **2020**, *59*, 16357; b) K. Kubota, Y. Pang, A. Miura, H. Ito, *Science* **2019**, *366*, 1500; c) J. A. Leitch, D. L. Browne, *Chem. - Eur. J.* **2021**, *27*, 9721.
[10] W. Feng, J. Yuan, L. Zhang, W. Hu, Z. Wu, X. Wang, X. Huang, P. Liu, S. Zhang, *Appl. Catal. B: Environ.* **2020**, *277*, 119250.
[11] K. Fan, C. Yu, S. Cheng, S. Lan, M. Zhu, *Surf. Interfaces* **2021**, *26*, 101335.
[12] H. Lei, Q. He, M. Wu, Y. Xu, P. Sun, X. Dong, *J. Hazard. Mater.* **2022**, *421*, 126696.
[13] J. Wu, N. Qin, E. Lin, B. Yuan, Z. Kang, D. Bao, *Nanoscale* **2019**, *11*, 21128.
[14] a) H. Liu, L. Li, C. Guo, J. Ning, Y. Zhong, Y. Hu, *Chem. Eng. J.* **2020**, *385*, 123929; b) C. Bie, B. Zhu, F. Xu, L. Zhang, J. Yu, *Adv. Mater.* **2019**, *31*, 1902868; c) L. Yin, X. Hai, K. Chang, F. Ichihara, J. Ye, *Small* **2018**, *14*, 1704153; d) J. Yi, T. Fei, L. Li, Q. Yu, S. Zhang, Y. Song, J. Lian, X. Zhu, J. Deng, H. Xu, *Appl. Catal. B: Environ.* **2021**, *281*, 119475; e) Y. Sheng, W. Li, Y. Zhu, L. Zhang, *Appl. Catal. B: Environ.* **2021**, *298*, 120585.
[15] Y. Liu, G. Zhu, J. Peng, J. Gao, C. Wang, P. Liu, *J. Mater. Sci.: Mater. Electron.* **2017**, *28*, 2172.
[16] M. M. Krzmanc, N. Daneu, A. Contala, S. Santra, K. M. Kamal, B. Likozar, M. Spreitzer, *ACS Appl. Mater. Interf.* **2021**, *13*, 370.
[17] a) R.-X. Wang, Q. Zhu, W.-S. Wang, C.-M. Fan, A.-W. Xu, *New J. Chem.* **2015**, *39*, 4407; b) Y. Ma, H. Luo, X. Zhou, R. Guo, F. Dang, K. Zhou, D. Zhang, *Nanoscale* **2020**, *12*, 8230.
[18] G. Guan, G. Gao, J. Xiang, J. Yang, L. Gong, X. Chen, Y. Zhang, K. Zhang, X. Meng, *ACS Appl. Nano Mater.* **2020**, *3*, 8424.
[19] a) S. Adireddy, C. Lin, B. Cao, W. Zhou, G. Caruntu, *Chem. Mater.* **2010**, *22*, 1946; b) O. El-Sayed, W. Mousa, A. Zeinert, A. Lahmar, M. El Marssi, I. Battisha, *Adv. Nat. Sci.: Nanosci. Nanotechnol.* **2020**, *11*, 015015.
[20] a) Y. Feng, L. Ling, Y. Wang, Z. Xu, F. Cao, H. Li, Z. Bian, *Nano Energy* **2017**, *40*, 481; b) E. Lin, J. Wu, N. Qin, B. Yuan, D. Bao, *Catal. Sci. Technol.* **2018**, *8*, 4788; c) W. Ma, B. Yao, W. Zhang, Y. He, Y. Yu, J. Niu, *Chem. Eng. J.* **2021**, *415*, 129000; d) J.-T. Lee, M.-C. Lin, J. M. Wu, *Nano Energy* **2022**, *98*, 107280; e) J. Zhang, Q. Bai, X. Bi, C. Zhang, M. Shi, W. Y. William, F. Du, L. Wang, Z. Wang, Z. Zhu, *Nano Today* **2022**, *43*, 101429.
[21] N. Alenzi, W.-S. Liao, P. S. Cremer, V. Sanchez-Torres, T. K. Wood, C. Ehlig-Economides, Z. Cheng, *Int. J. Hydrog. Energy* **2010**, *35*, 11768.
[22] Y. Zhao, X. Huang, F. Gao, L. Zhang, Q. Tian, Z.-B. Fang, P. Liu, *Nanoscale* **2019**, *11*, 9085.
[23] X. Xu, L. Xiao, Z. Wu, Y. Jia, X. Ye, F. Wang, B. Yuan, Y. Yu, H. Huang, G. Zou, *Nano Energy* **2020**, *78*, 105351.
[24] H. You, Z. Wu, L. Zhang, Y. Ying, Y. Liu, L. Fei, X. Chen, Y. Jia, Y. Wang, F. Wang, *Angew. Chem.* **2019**, *131*, 11905.
[25] S. Li, Z. Zhao, D. Yu, J.-Z. Zhao, Y. Su, Y. Liu, Y. Lin, W. Liu, H. Xu, Z. Zhang, *Nano Energy* **2019**, *66*, 104083.
[26] a) L. Shi, C. Lu, L. Chen, Q. Zhang, Y. Li, T. Zhang, X. Hao, *J. Alloys Compd.* **2022**, *895*, 162591; b) Q. Zhou, N. Li, D. Chen, Q. Xu, H. Li, J. He, J. Lu, *Chem. Eng. Sci.* **2022**, *247*, 116707.
[27] Y. Abdollahi, A. H. Abdullah, U. I. Gaya, S. Ahmadzadeh, A. Zakaria, K. Shameli, Z. Zainal, H. Jahangirian, N. A. Yusof, *J. Braz. Chem. Soc.* **2012**, *23*, 236.
[28] a) S. Tu, H. Huang, T. Zhang, Y. Zhang, *Appl. Catal. B: Environ.* **2017**, *219*, 550; b) E. Lin, Z. Kang, J. Wu, R. Huang, N. Qin, D. Bao, *Appl. Catal. B: Environ.* **2021**, *285*, 119823; c) C. Hu, H. Huang, F. Chen, Y. Zhang, H. Yu, T. Ma, *Adv. Funct. Mater.* **2020**, *30*, 1908168.
[29] B. Li, C. Lai, M. Zhang, S. Liu, H. Yi, X. Liu, N. An, X. Zhou, L. Li, Y. Fu, *Chem. Eng. J.* **2021**, *409*, 128281.
[30] B. Yang, X. Cheng, Y. Zhang, W. Li, J. Wang, Z. Tian, E. Du, H. Guo, *J. Hazard. Mater.* **2021**, *407*, 124853.
[31] S. Padmaja, S. A. Madison, *J. Phys. Org. Chem.* **1999**, *12*, 221.
[32] F. Mushtaq, X. Chen, H. Torlakcik, C. Steuer, M. Hoop, E. C. Siringil, X. Marti, G. Limburg, P. Stipp, B. J. Nelson, *Adv. Mater.* **2019**, *31*, 1901378.

